Synthesis of Atomically Thin Transition Metal Disulfides for Charge Transport Layers in Optoelectronic Devices

Ki Chang Kwon,[†] Cheolmin Kim,[‡] Quyet Van Le,[‡] Seungo Gim,[§] Jong-Myeong Jeon,[†] Ju Young Ham,[§] Jong-Lam Lee,[*,§] Ho Won Jang,[*,†] and Soo Young Kim[*,‡]

[†]Department of Materials Science and Engineering, Research Institute of Advanced Materials, Seoul National University, Seoul 151-744, Republic of Korea, [‡]School of Chemical Engineering and Materials Science, Chung-Ang University, Seoul 156-756, Republic of Korea, and [§]Department of Materials Science, Pohang University of Science and Technology (POSTECH), Pohang, Gyeongbuk 790-784, Republic of Korea

ABSTRACT Metal sulfides (MeS_2) such as MoS_2 and WS_2 were used as charge transport layers in organic light-emitting diodes (OLEDs) and organic photovoltaic (OPV) cells in order to enhance the stability in air comparing to poly(3,4-ethylenedioxythiophene):poly-(styrenesulfonate) (PEDOT:PSS). MeS_2 layers with a polycrystalline structure were synthesized by a chemical deposition method using uniformly spin-coated $(NH_4)MoS_4$ and $(NH_4)WS_4$ precursor solutions. The ultraviolet-ozone (UV-O_3) treatment on MeS_2 leads to the removal of the surface contaminants produced by the transfer process, resulting in a uniform surface and an increase of the work function. The maximum luminance efficiencies of the OLEDs with UV-O_3-treated MoS_2 and WS_2 were 9.44 and 10.82 cd/A, respectively. The power conversion efficiencies of OPV cells based on UV-O_3-treated MoS_2 and WS_2 were 2.96 and 3.08%, respectively. These values correspond to over 95% of those obtained with (PEDOT:PSS) based devices. Furthermore, OLEDs and OPV cells based on MeS_2 showed two to six times longer stability in air compared with PEDOT:PSS based devices. These results suggest that UV-O_3-surface-treated MeS_2 could be a promising candidate for a charge transport layer in optoelectronic devices.

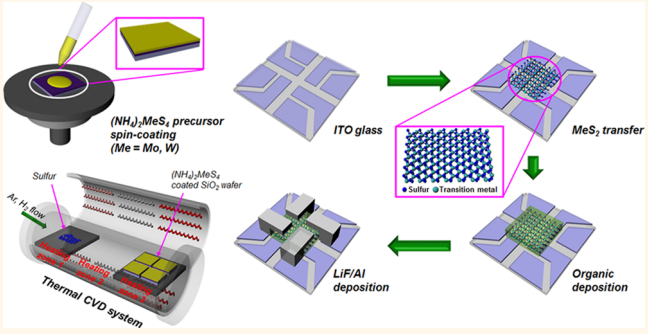

KEYWORDS: transition metal disulfide · chemical vapor deposition · organic light-emitting diodes · organic photovoltaics · hole injection layer

Transition metal dichalcogenides (TMDCs) have attracted increasing attention because of their great potential as catalysts of hydrogen evolution reactions as well as their application in energy storage, memory and logic devices, and optoelectronic devices, because of their high on/off current ratio, high carrier mobility, and semiconducting properties.[1−6] TMDCs with transition metals from groups IV−VII of the periodic table are predominantly layered, whereas some of the TMDCs with metals from the groups VIII−X of the periodic table are commonly found in nonlayered structures. The graphite-like layered structure of the TMDCs leads to a strong anisotropy in the electrical, chemical, mechanical, and thermal properties of the TMDCs. Theoretical and experimental studies reported several advantages of isolated monolayers of TMDCs.[7−10] First, the lone-pair electrons of the chalcogen atoms in the isolated monolayer structure enable ballistic transport, indicating that the carrier mobility can be improved.[7] Second, the indirect-to-direct band gap transition from bulk to monolayer material induces quantum confinement effects. Therefore, the photoluminescence properties of MoS_2 and WS_2 monolayers are strongly enhanced, whereas only weak emission is observed in the multilayered form.[8,9] Lastly, the typical band gap of the monolayer is approximately 50% larger than that of the bulk form.[10]

* Address correspondence to jllee@postech.ac.kr, hwjang@snu.ac.kr, sooyoungkim@cau.ac.kr.

Received for review January 14, 2015 and accepted March 22, 2015.

Published online March 22, 2015
10.1021/acsnano.5b01504

Owing to the advantages of monolayer TMDCs, many researchers try to exfoliate bulk TMDCs to a monolayer and synthesize monolayers of TMDCs using precursor materials. Liquid exfoliation and alkali metal complex intercalations have been widely used to exfoliate each layer of the TMDCs.[11,12] However, the products obtained by these methods tend to assume zero- (fullerene-like nanoparticles) or one-dimensional (nanotube structures) structures.[13] Furthermore, the quality of the TMDC products is not good enough compared with that of those obtained by a mechanical exfoliation method, albeit the solution process has the potential for mass production. For these reasons, the chemical vapor deposition (CVD) method with sulfur powder and precursors is introduced to synthesize TMDCs with high quality and on a large scale.[13−17] However, to enable the wide application of TMDCs, the growth technique of TMDCs with few layers still needs to be improved in relation to the domain size, crystal quality, and thickness control.[18]

The well-known poly(3,4-ethylenedioxythiophene): poly(styrenesulfonate) (PEDOT:PSS), widely used as a hole injection layer (HIL) or hole extraction layer (HEL), has several disadvantages such as hygroscopic properties (damages to organic layers) and a highly acidic suspension (pH $\approx$ 1; corrosion of indium−tin oxide (ITO)), which result in a poor stability in air.[19] Metal oxides (MeO_3) such as molybdenum oxide (MoO_3) and tungsten oxide (WO_3) were also used as HIL or HEL for enhancing the stability of the optoelectronic devices. However, the thermal deposition of MoO_3 and WO_3 produced a partially amorphous region, inducing the dangling bonds which facilitate the reaction of the organic materials and deteriorating the device performance.[20,21] In TMDCs, the oxidation state of the Mo and W atoms is +4 and that of the S atom is −2, meaning that MeS_2 (Me = Mo or W) is terminated with S atoms on the upper and lower side. The lone-pair electrons on the surfaces and the absence of dangling bonds in MoS_2 and WS_2 layers enhance the stability against reactions with other chemical species. As a result, MoS_2 and WS_2 are expected to be quite good candidates as HILs or HELs in optoelectronic devices such as organic light-emitting diodes (OLEDs) and organic photovoltaic (OPV) cells.

In this work, we introduced ultraviolet-ozone (UV-O_3) treated MoS_2 and WS_2 in OLEDs and OPV cells as a HIL and HEL to enhance the stability in air comparting to PEDOT:PSS. MoS_2 and WS_2 were synthesized on a SiO_2/Si substrate using spin-coated $(NH_4)_2MoS_4$ and $(NH_4)_2WS_4$ precursors. The use of UV-O_3-treated MoS_2 and WS_2 in OLEDs and OPV cells is discussed on the basis of the obtained experimental results and measurements. It is shown that UV-O_3-surface-treated MeS_2 could be a promising candidate for a charge transport layer in optoelectronic devices.

RESULTS AND DISCUSSION

Synthesis of the MeS_2 Layers and Fabrication of the Devices. The TMDCs were synthesized using $(NH_4)_2MoS_4$ or $(NH_4)_2WS_4$ as a precursor. The thermolysis at 500 °C under N_2 atmospheric conditions converted the precursors to MoS_x and WS_x thin layers. The conversion of MoS_x and WS_x thin layers to MoS_2 and WS_2 thin films occurred at a temperature above 900 °C in the presence of H_2 gas, as described by the following equations.[22,23]

$$(NH_4)_2MeS_4 + H_2 \rightarrow 2NH_3 + H_2S + MeS_3 \text{ (below 500°C, Me = Mo, W)} \quad (1)$$

$$MeS_3 + H_2 \rightarrow MeS_2 + H_2S \text{ (above 900°C)} \quad (2)$$

We have investigated the thermolysis of a series of ammonium thio-transition metal complexes by using a thermal CVD system. Figure 1(a,b) shows how to synthesize the MoS_2 and WS_2 thin layers by using our CVD thermolysis method. Highly pure $(NH_4)_2MeS_4$ (Me = Mo, W, purchased from Sigma-Aldrich, purity of 99.99%) was dissolved in ethylene glycol with a concentration equal to 5 mM. The selection of a well-coordinated solvent is important to obtain uniform precursor layers that are converted to TMDCs layers. The solution was sonicated for 10 min before spin coating on a 300 nm-thick SiO_2/Si substrate. The SiO_2/Si substrate was cleaned with a piranha solution (H_2SO_4/H_2O_2 = 1:1), acetone, isopropyl alcohol, and deionized (DI) water for 10 min in regular sequence. Then, the substrate was blown with N_2 gas and baked on a hot plate at 120 °C for 10 min. To obtain a uniform layer of the precursor solution, the substrate was treated with O_2 plasma and UV-O_3 for 15 min. Additional information on the substrate treatment is discussed in Supporting Information, Figure S1. The thermal annealing process was performed in three different parts of the hot zone of the CVD system. The small amounts of sulfur powder and the SiO_2 wafers spin-coated with the precursors were located at the heating zones 1 and 3 in Figure 1(b), respectively. Further synthesis and transfer techniques are discussed in the Methods section. The MeS_2 floated on water and the MeS_2 transferred on a flexible substrate are shown in Supporting Information, Figure S2. The fabrication sequence of MeS_2 HIL/HEL based OLED/OPV devices is shown in Figure 1(c): (i) cleaning of the ITO electrode with acetone, isopropyl alcohol, and DI water; (ii) MeS_2 transfer (Me = Mo, W); (iii) deposition of the organic layer; (iv) deposition of the LiF/Al electrode. After the fabrication, the optoelectronic device properties were measured, and the devices were put under atmospheric conditions to perform the stability measurements.

Characteristics of the Synthesized MeS_2 Layers. The field-emission scanning electron microscopy (FE-SEM) images of MoS_2 and WS_2 are shown in Figure 2(a,b).

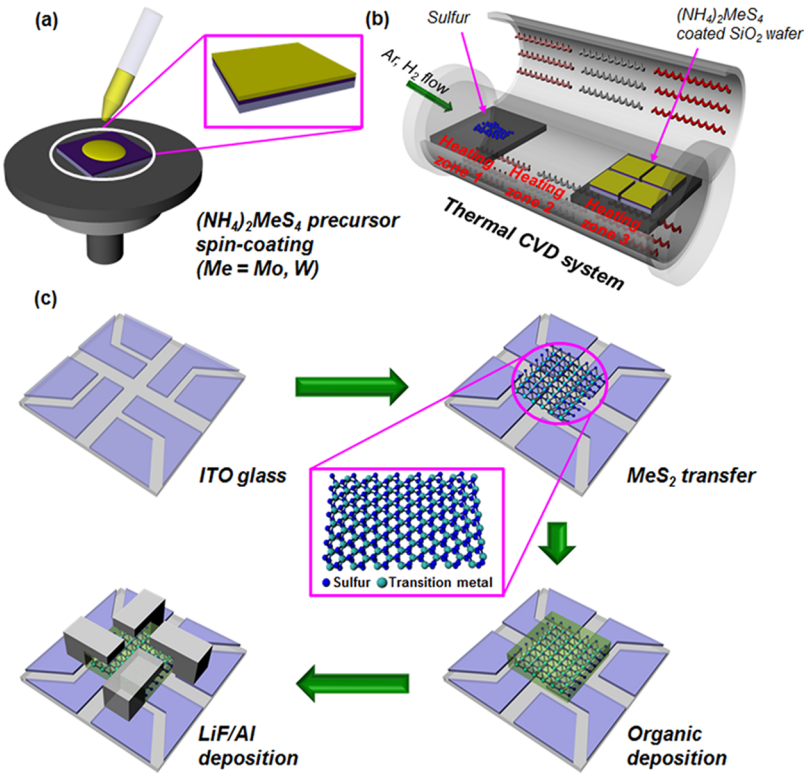

Figure 1. Schematic illustration of the synthesis of MoS_2 and WS_2, and their application to optoelectronic devices. (a) The preparation of the substrate using $(NH_4)_2MoS_4$ and $(NH_4)_2WS_4$ precursors. (b) Synthesis of MoS_2 and WS_2 layers by using a thermal CVD system. (c) Fabrication procedure of OLED and OPV devices with MeS_2 HIL or HEL.

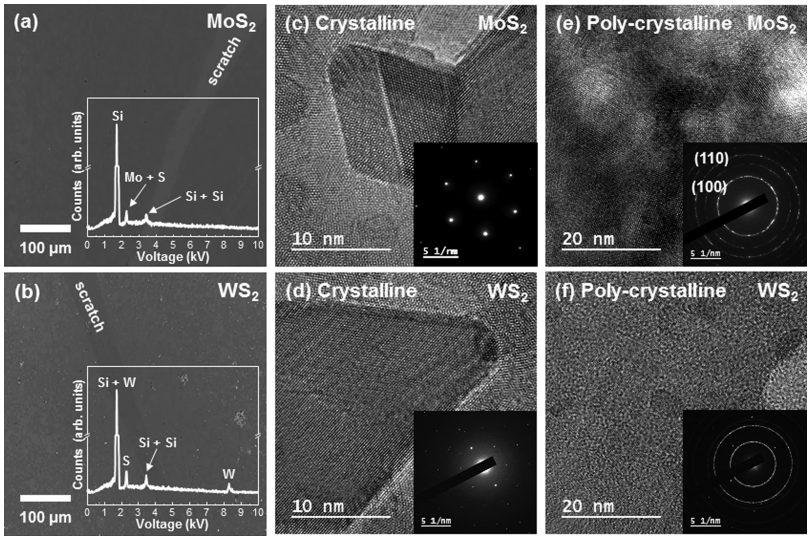

Figure 2. Microscopic analysis of synthesized MoS_2 and WS_2 layers. FE-SEM images and EDS spectra of (a) MoS_2 and (b) WS_2 layers. The EDS spectra show the presence of specific metal and sulfur atoms on the synthesized MoS_2 and WS_2 layers. HR-TEM images and SAED patterns are shown for (c) crystalline-MoS_2, (d) crystalline-WS_2 layer, (e) polycrystalline region of MoS_2, and (f) polycrystalline region of the WS_2 sheet.

Scratches are intentionally made to confirm the presence of MeS_2. The surface of MeS_2 is smooth. The energy dispersive spectroscopy (EDS) spectra show the specific peaks of molybdenum, tungsten, and sulfur, confirming that the synthesized films are MoS_2 and WS_2. Figure 2(c−f) shows the high-energy transmission electron microscopy (HR-TEM) images of MoS_2 and WS_2. The periodic atomic arrangements of the MeS_2 films are shown in Figure 2(c,d). Furthermore, the selected area electron diffraction (SAED) patterns reveal a hexagonal structure. These results indicate that single-crystalline MeS_2 layers were synthesized.[24] However, a nonperiodic atomic arrangement in the HR-TEM images and ring motifs in the SAED patterns

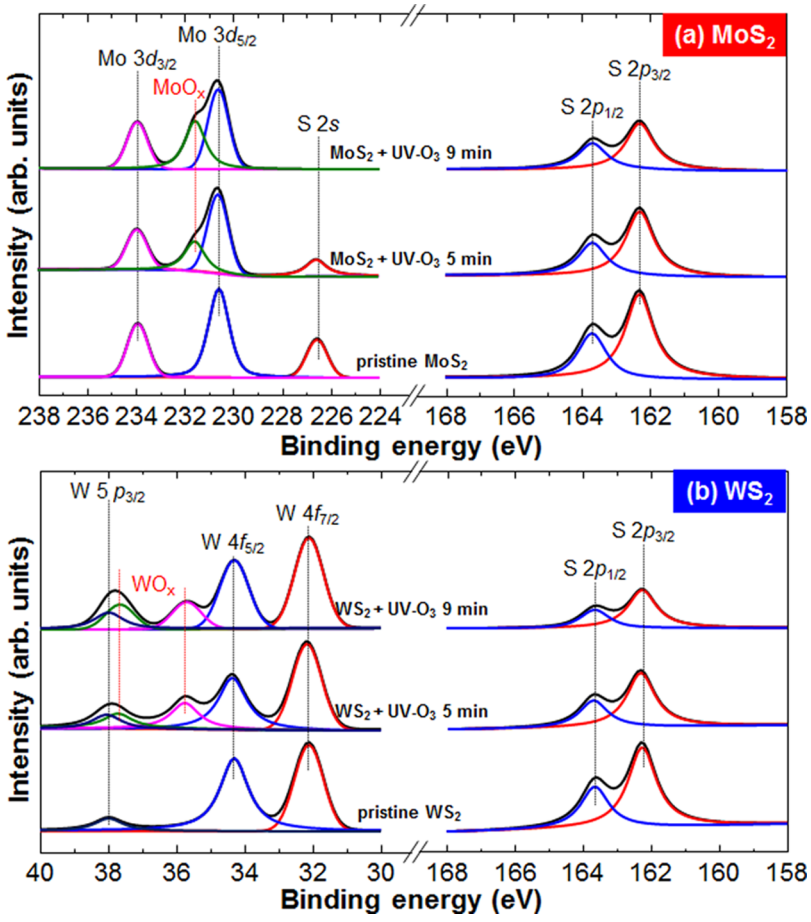

Figure 3. SRPES analysis of pristine and UV-O_3-exposed MoS_2 and WS_2. SRPES core level spectra of (a) Mo 3*d*, S 2*p*, and (b) W 4*f*, S 2*p*. After the UV-O_3 oxidation, the transition metal oxide peak appeared and the intensity of the sulfur peak decreased.

are also found, as shown in Figure 2(e,f), indicating the presence of polycrystalline areas in the synthesized MoS_2 and WS_2 layers. These data are consistent with previous reports that discussed the lower crystalline properties of MoS_2 and WS_2 synthesized on a SiO_2/Si wafer compared with MeS_2 synthesized on a sapphire substrate.[25] Therefore, MoS_2 and WS_2 with few layers and polycrystalline structure were synthesized by using uniformly spin-coated $(NH_4)MoS_4$ and $(NH_4)WS_4$ precursor solutions.

Figure 3(a,b) shows the Mo 3*d*, W 4*f*, and S 2*p* synchrotron radiation photoemission spectroscopy (SRPES) spectra of the MoS_2 and WS_2 layers as a function of the UV-O_3 treatment time. The survey scans of both MoS_2 and WS_2 are shown in Supporting Information, Figure S3. Five peaks appear at 162.3, 163.8, 226.5, 230.5, and 234.0 eV in the MoS_2 sample, which are assigned to S $2p_{3/2}$, S $2p_{1/2}$, S 2*s*, Mo $3d_{5/2}$, and Mo $3d_{3/2}$, respectively. In the case of the WS_2 sample, the W-related peaks of W $4f_{7/2}$, W $4f_{5/2}$, and W $5p_{3/2}$ are shown at 32.0, 34.4, and 38.0 eV, respectively. These results are consistent with the findings of previous reports on MoS_2 and WS_2 crystals.[26,27] As the UV-O_3 treatment time increased, the peak intensity of S 2*s* in the MoS_2 layer progressively decreased until the peak finally disappeared. Furthermore, the Mo−O and W−O bonds were observed, and their intensities increased as a function of the UV-O_3 treatment time. The intensities of the S 2*p* peaks also decreased after the UV-O_3 treatment. The O 1*s* peak was depicted in Supporting Information, Figure S4. In the case of the MoS_2 layers, the intensity ratio of the O−S bond to the O−Si bond increased from 0 to 0.12 and 0.19 after 5 and 9 min of UV-O_3 treatment, respectively. Similarly, in the case of the WS_2 layers, the ratio increased from 0.05 to 0.13 and 0.21 after 5 and 9 min of UV-O_3 treatment, respectively. The atomic percentages of Mo, W, and S slightly decreased from 33.6, 31.6, and 61.3% to 28.2, 27.6, and 57.9%, respectively, after 9 min of UV-O_3 treatment. However, the atomic concentration of O 1s dramatically increased from 5.2 and 8.2% to 14.0 and 16.3% for MoS_2 and WS_2, respectively, after the UV-O_3 surface treatment, as shown in Supporting Information, Figure S5. These data indicate that some portions of the MeS_2 surface changed from sulfide to oxide. The decrease of the water contact angle after the UV-O_3 treatment supports this assumption, as shown in Supporting Information, Figure S6.

Figure 4(a,b) shows the Raman spectra of pristine and UV-O_3-treated MoS_2 and WS_2 layers. The Raman

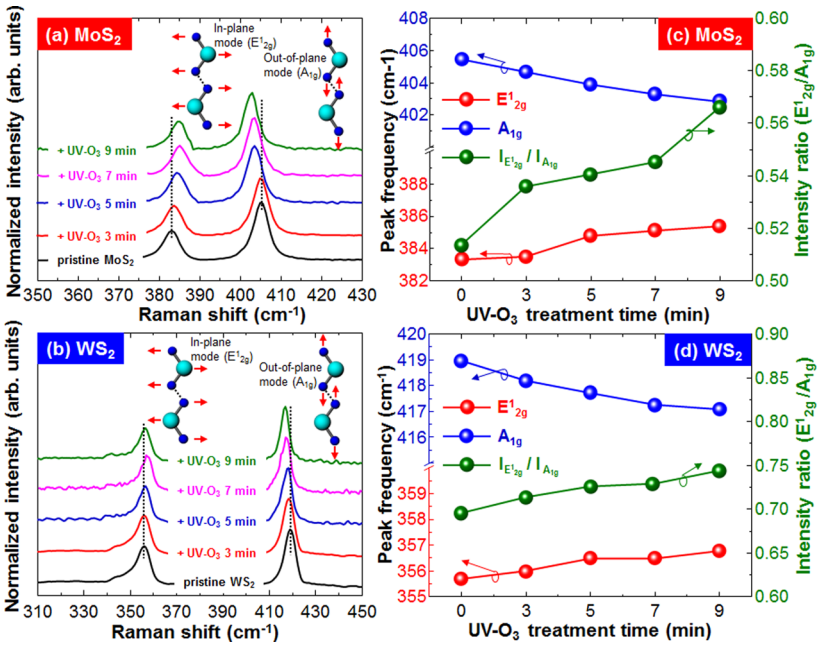

Figure 4. Raman spectroscopy analysis of pristine and UV-O_3-treated MoS_2 and WS_2. Raman spectra of pristine MeS_2: (a) MoS_2 and (b) WS_2, at different UV-O_3 surface treatment times. For both MoS_2 and WS_2, the peak position of E^1_{2g} and A_{1g} shifted to higher and lower wave numbers, respectively, as a function of the UV-O_3 exposure time. The shifted peak position and intensity ratio of E^1_{2g} to A_{1g} are shown in (c) MoS_2, and (d) WS_2.

spectra of the TMDCs appear to contain two predominant peaks: (i) the out-of-plane (A_{1g}) mode where the top and bottom chalcogen atoms are moving out of the plane in opposite directions while the transition metal is stationary; (ii) the in-plane (E^1_{2g}) mode where both the transition metal and chalcogen atoms are moving in-plane in opposite directions.[28−30] The in-plane and out-of-plane mode of the TMDCs are drawn in the inset of Figure 4(a,b). The E^1_{2g} peak of pristine MoS_2 was revealed at 383.3 cm^{-1} and blue-shifted to 383.5, 384.7, 385.1, and 385.4 cm^{-1} after UV-O_3 treatment for 3, 5, 7, and 9 min, respectively. The A_{1g} peak of pristine MoS_2 was revealed at 405.4 cm^{-1} and red-shifted to 404.6, 403.9, 403.2, and 402.8 cm^{-1} after the same UV-O_3 treatments, respectively. A similar tendency of peak shift was observed in the case of WS_2. The peak shift data and the change of the intensity ratio of E^1_{2g} and A_{1g} are summarized in Figure 4(c,d). Both the peak positions of E^1_{2g} and A_{1g} shifted to a higher and lower wavenumber, and the E^1_{2g} to A_{1g} peak intensity ratio increased after the UV-O_3 treatment on the MeS_2 layers. It has been reported that the addition of extra layers on TMDC leads to the stiffening of the out-of-plane phonon modes and relaxation of the in-plane bonding, resulting in a blue-shift of the A_{1g} mode and red-shift of the E^1_{2g} mode.[28] Therefore, the decrease in distance between E^1_{2g} and A_{1g} suggests the removal of surface contaminants, resulting in the thinning and flattening of the MeS_2 layer. Furthermore, it has been reported that the E^1_{2g} to A_{1g} peak intensity ratio value decreases as the number of TMDC layers increases.[29,30] Thus, the increase of the E^1_{2g} to A_{1g} peak intensity ratio shown in Figure 4(c,d) suggests that the thickness of the MeS_2 layer decreased with the UV-O_3 treatment. According to the atomic force microscopy (AFM) analysis shown in Supporting Information, Figure S7, the thickness of MoS_2 and WS_2 decreased from 2.0 and 1.8 nm to 1.5 and 1.2 nm, respectively, after UV-O_3 treatment for 5 min. Therefore, the UV-O_3 treatment on MeS_2 leads to the removal of the surface contaminants induced by the transfer process, producing a uniform surface.

OLED and OPV Characteristics. The structure of the OLED with MeS_2 HIL and the schematic band diagram are depicted in Figure 5(a). The energy levels of ITO, PEDOT:PSS, (*N*,*N*′-Di(1-naphthyl)-*N*,*N*′-diphenyl-(1,1′-biphenyl)-4,4′-diamine) (NPB), (Tris(8-hydroxyquinoline)-aluminum) (Alq_3), 2,3,6,7-tetrahydro-1,1,7,7,-tetramethyl-1*H*,5*H*,11*H*-10-(2-benzothiazolyl) quinolizine-[9,9a,1gh] (C545T), bathocurione (BCP), and LiF/Al were obtained from the literature.[31] The values of the work function of MoS_2 and WS_2 were measured by ultraviolet photoemission spectroscopy (UPS), as shown in Supporting Information, Figure S8. The work functions increased from 4.6 and 4.75 eV to 4.8 and 4.95 eV for MoS_2 and WS_2, respectively, after UV-O_3 treatment for 5 min. This means that, among all the samples, the lowest hole injection barrier belongs to UV-O_3-treated WS_2. Figure 5(b−e) shows the current density−voltage, luminance−voltage, luminance efficiency−current density, and power efficiency−current density characteristics of the OLEDs with PEDOT:PSS, pristine MeS_2, UV-O_3-exposed MeS_2 and MeO_3. The thickness of MeO_3 is fixed at 3 nm following to the thickness of MeS_2.

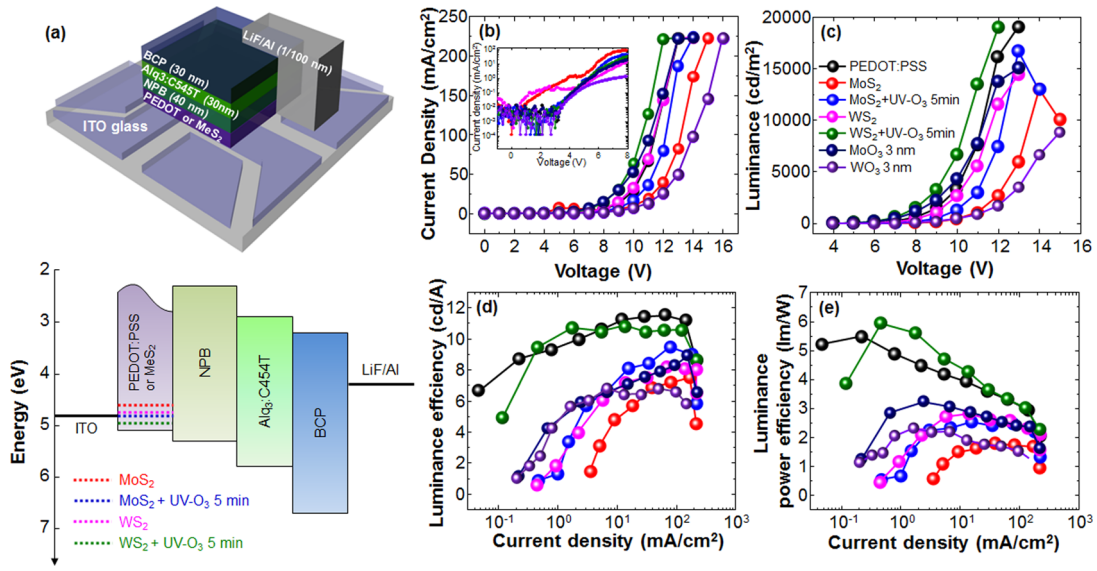

Figure 5. Device characteristics of pristine MeS_2, UV-O_3 treated MeS_2, and MeO_3-based OLEDs. (a) The illustration of OLED device structure of MoS_2 and WS_2 HIL with UV-O_3 exposure. Schematic energy band diagram is also shown. (b) Current density−voltage, (c) luminance−voltage, (d) luminance efficiency−current density, and (e) luminance power efficiency−current density characteristics of OLEDs. The current density−voltage curve at low voltage region is magnified in the inset of (b).

TABLE 1. Summary of the Device Characteristics of Pristine MeS_2, UV-O_3-Treated MeS_2, and MeO_3 HIL Based OLEDs

HIL	turn-on voltage[a] (V)	luminance$_{max}$ (cd/m^2)	luminance Eff$_{max}$ (cd/A)	power Eff$_{max}$ (lm/W)	CIE1931 coordinates[b] (*x*, *y*)
PEDOT:PSS	4.4	19 000	11.42	5.48	(0.32, 0.65)
pristine MoS_2	6.4	13 000	7.51	1.8	(0.32, 0.65)
MoS_2 + UV-O_3 5 min	5.65	16 700	9.44	2.53	(0.32, 0.64)
pristine WS_2	5.1	14 400	8.14	2.81	(0.33, 0.64)
WS_2 + UV-O_3 5 min	4.1	19 000	10.82	5.92	(0.33, 0.64)
MoO_3 3 nm	4.25	15 000	9.03	3.21	(0.31, 0.65)
WO_3 3 nm	5.4	8 810	6.99	2.31	(0.33, 0.63)

[a] Measured at 10 cd/m^2. [b] Recorded at maximum luminance.

The OLED with UV-O_3-treated MeS_2 performs better than that with pristine MeS_2 and MeO_3. The inset graph of Figure 5(b) shows the log-scaled leakage current at low voltage region. The leakage current shown in OLEDs based on pristine MeS_2 disappeared in OLEDs based on UV-O_3 treated MeS_2. It is considered that decrease of surface roughness and removal of contaminant on pristine MeS_2 layers after UV-O_3 treatment got rid of leakage current. The optimized UV-O_3 treatment lasted for 5 min because of the surface damage induced from UV-O_3, as shown in Supporting Information, Figures S9−S11. The OLED with UV-O_3-exposed WS_2 shows the lowest turn-on voltage, 4.1 V, and the brightest luminance value, 19 000 cd/m^2; these values are comparable with those obtained from the PEDOT:PSS-based device (4.4 V and 19 000 cd/m^2) and better than MeO_3-based device (4.25 V and 15 000 cd/m^2 for MoO_3, 5.4 V and 8810 cd/m^2 for WO_3). The best luminance efficiency and power efficiency of the OLEDs based on UV-O_3-treated WS_2 are approximately equal to 95 and 109% than those obtained from of the OLEDs based on PEDOT:PSS. The detailed OLED characteristics are summarized in Table 1, Table S1, and S2.

MeS_2 was used in OPV cells as HEL, as shown in Figure 6. Figure 6(a) shows the device structure and energy band diagram. The energy levels of ITO, PEDOT:PSS, poly(3-hexylthiophene) (P3HT), [6,6]-phenyl C_{61} butyric acid methyl ester ($PC_{60}BM$), and LiF/Al were obtained from the literature.[32] The transmittance of each sample was measured by using UV−visible spectra as shown in Figure 6(b). The transmittance at 550 nm of MeS_2 layers slightly elevated from 91.7 to 94.0% for MoS_2, and from 92.4 to 94.6% for WS_2 after UV-O_3 treatment for 5 min. The device current density−voltage characteristics are shown in Figure 6(c). The open-circuit voltage (V_{oc}), short-circuit current (J_{sc}), fill factor (FF), and power conversion efficiency (PCE) of the reference (PEDOT:PSS) are 0.61 V, 8.27 mA/cm^2, 64.2, and 3.23%, respectively. The efficiency of the UV-O_3-treated MeS_2-based devices varied from 2.72 to 2.96% for MoS_2 HEL, and from 2.79 to 3.08% for WS_2 HEL at different UV-O_3 exposure times, as shown in Supporting Information, Figure S12. The devices with MeS_2 treated by UV-O_3 for 5 min show the best efficiency: V_{oc} = 0.60 V, J_{sc} = 7.81 mA/cm^2, FF = 63.6, and PCE = 2.96% for MoS_2; V_{oc} = 0.61 V, J_{sc} = 7.87 mA/cm^2, FF = 64.1, and PCE = 3.08%

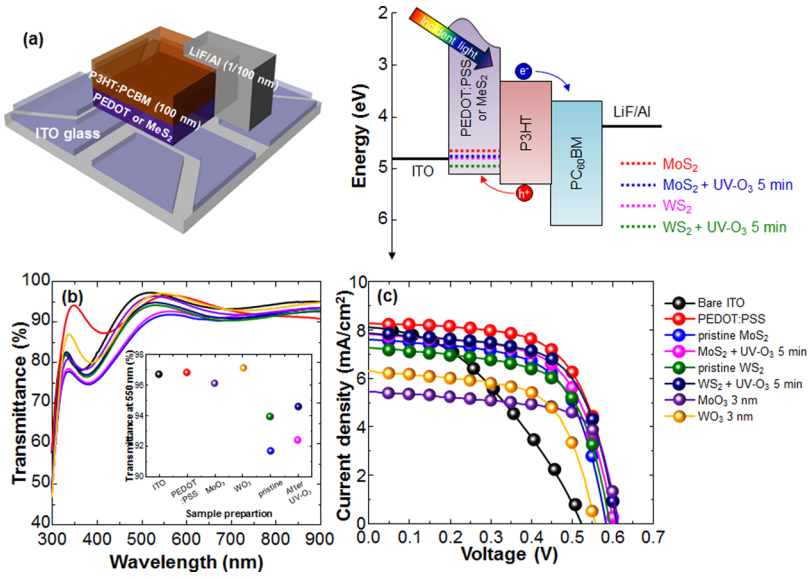

Figure 6. Device characteristics of pristine MeS_2, UV-O_3 treated MeS_2, and MeO_3-based OPVs. (a) Illustration of the OPV device structure of MoS_2 and WS_2 HEL with UV-O_3 exposure. Schematic energy band diagram is also shown. (b) The transmittance spectra of bare ITO, PEDOT:PSS, pristine MeS_2, UV-O_3-treated MeS_2, and MeO_3 layers. The transmittance values at 550 nm are shown in the inset graph of (b). (c) Current density−voltage curves of OPV devices. The OPV based on UV-O_3-exposed WS_2 sample shows the best performance among all the samples.

TABLE 2. Summary of the Device Characteristics of Pristine MeS_2, UV-O_3-Exposed MeS_2, and MeO_3 HEL Based OPV Cells

HEL	J_{sc} (mA/cm^2)	V_{oc} (V)	FF	PCE (%)	R_{sh}[a] (Ω cm^2)
bare ITO	8.10	0.52	0.40	1.70	12 725.67
PEDOT:PSS	8.27	0.61	0.64	3.23	36 543.93
pristine MoS_2	7.24	0.59	0.63	2.72	21 689.53
MoS_2 + UV-O_3 5 min	7.81	0.60	0.63	2.96	40 068.85
pristine WS_2	7.61	0.59	0.63	2.79	23 866.64
WS_2 + UV-O_3 5 min	7.87	0.61	0.64	3.08	36 149.29
MoO_3 3 nm	6.29	0.61	0.68	2.29	18 251.37
WO_3 3 nm	5.45	0.56	0.63	2.20	16 589.19

[a] R_{sh}: shunt resistance.

for WS_2. The changes of J_{sc} and PCE were attributed to the increase of transmittance, variation of the work function, and the removal of the surface contamination from the MeS_2 layer by UV-O_3 treatment. The decrease of the device performance for UV-O_3 exposure times longer than 5 min is due to the surface damage. The detailed OPV characteristics are summarized in Table 2, Table S3, and S4. These data suggest that the MeS_2 layer may be used as HIL or HEL in organic devices instead of PEDOT:PSS.

Device Stability Test under Ambient Air. In order to investigate the stability of OLED and OPV devices with UV-O_3-treated MeS_2, the lifetimes were evaluated in air conditions at 25 °C and 50% humidity. Figure 7(a) shows the illumination images of each different OLED device as a function of the keeping time. The illumination images were captured at the applied current density of 100 mA/cm^2. All the samples progressively degrade because of the moisture. In the case of the PEDOT:PSS-based OLED, the illumination dramatically decreased after exposure for 4 h and the device ceased operating after 6 h. However, the OLEDs based on pristine and UV-O_3-treated MeS_2 layers are shown to be operative even after 6 h under the same conditions. Thus, the device stability of OLEDs based on MeS_2 is superior to that of the OLEDs based on PEDOT:PSS. The voltage changes of the OLEDs as a function of the keeping time in air are shown in Figure 7(b) for MoS_2 and Figure 7(c) for WS_2. The voltage changes at 100 mA/cm^2 dramatically increased to 180% in the PEDOT:PSS-based OLED after 6 h. However, the voltage change of the OLED based on MeS_2 is lower than that of the OLED based on PEDOT:PSS. Notably, OLEDs with UV-O_3-treated MeS_2 show a smaller voltage variation than the OLEDs with pristine MeS_2. The effect of the MeS_2 layers on the air stability of the OPV cells is shown in Figure 7(d). The PCE value is normalized with respect to the PEDOT:PSS-based OPV cell. The time required to reach half of the PCE value is equal to 8, 16, 21, 16, 28, 24, 24 h for PEDOT:PSS, MoS_2, UV-O_3-treated MoS_2, WS_2, and UV-O_3-treated WS_2, MoO_3 and WO_3-based OPV cells, respectively. Although the PCE values of the MeS_2-based OPV cells are lower than those of the PEDOT:PSS-based cells, the stability is significantly improved. Furthermore, it is shown that the properties of OLEDs and OPVs based on UV-O_3-treated MeS_2 HIL are comparable to, or even better than, those of the OLEDs and OPVs based on MeO_3, which is reported as a good HIL. Hence, the MeS_2 layers are suitable for replacing the PEDOT:PSS layer, which is an acidic material and presents a high reactivity with the ITO layer.

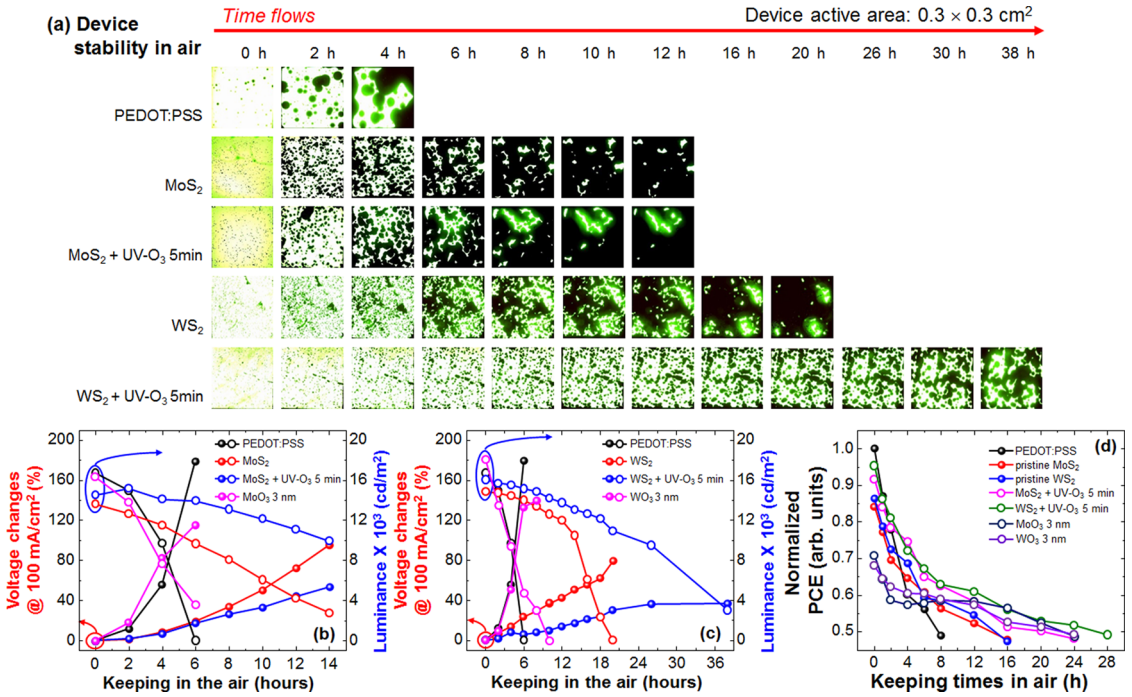

Figure 7. Device stability test results of pristine and UV-O_3-exposed MoS_2 and WS_2 HIL based OLEDs and OPV cells. (a) Illumination images of several types of samples including PEDOT:PSS, pristine MoS_2 and WS_2, UV-O_3 treated MoS_2 and WS_2 HIL. The device illumination size is 0.3 × 0.3 cm^2. Comparison between a PEDOT:PSS device and (b) MoS_2- and MoO_3-based cells and (c) WS_2- and WO_3-based cells; the variation of voltage changes at 100 mA/cm^2 (left column, red, closed circle) and luminance value (right column, blue, open circle) as a function of the time in air ambient. (d) The change of normalized PCE values as a function of keeping time in air ambient for the different sample types.

CONCLUSIONS

The hole injection and extraction properties of UV-O_3-treated MoS_2 and WS_2 in OLED and OPV devices were investigated in relation to the extended air stability. The MoS_2 and WS_2 layers were synthesized by thermolysis of a $[(NH_4)_2MoS_4]$ and $[(NH_4)_2WS_4]$ precursor solution with a two-step annealing process. The synthesized MoS_2 and WS_2 show a polycrystalline structure. According to SRPES and Raman spectra analyses, the UV-O_3 exposure modulated the work-function of MoS_2 and WS_2, as well as removed the surface contaminants. The maximum luminance efficiencies of OLEDs with UV-O_3-treated MoS_2 and WS_2 were 9.44 and 10.82 cd/A, respectively. The PCE values of UV-O_3-treated MoS_2 and WS_2-based OPV cells were 2.96 and 3.08%, respectively. These values correspond to over 95% of those obtained from PEDOT:PSS-based devices. Because of the removal of surface contaminants and the increased work function, the device performance was significantly enhanced after UV-O_3 exposure of MeS_2. Furthermore, the device stability in air significantly improved because of its nonacidic and chemically stable properties, which can be achieved by replacing conventional PEDOT:PSS with UV-O_3-exposed MoS_2 and WS_2 layers. Therefore, these results show that UV-O_3-treated MoS_2 and WS_2 under optimized conditions may replace the conventional PEDOT:PSS layer, enhancing the overall device reliability.

METHODS

Synthesis of MoS_2 and WS_2. The insulating substrates, SiO_2 (300 nm)/Si wafer, were prepared with a standard piranha solution and conventional cleaning procedures based on acetone, isopropyl alcohol, and DI water bath sonication. The precursor solution was prepared with a 5 mM concentration of $(NH_4)_2MoS_4$ and $(NH_4)_2WS_4$ in ethylene glycol. For the optimized precursor coating conditions, the cleaned substrates were subjected to O_2 plasma and UV-O_3 surface treatment for 15 min. The substrates were spin coated with the precursor solutions at 3500 rpm for 60 s. For the thermolysis of the precursor films, a thermal CVD system involving high purity hydrogen (H_2) and nitrogen (N_2) gas was used. First, the temperature of the CVD furnace was set to 500 °C for 30 min, under H_2 and N_2 gas flow at 1 Torr pressure. The H_2 and N_2 flow rate were controlled by mass flow controllers for a rate of 40 (H_2) and 200 (N_2) cm^3/min. Then, the thermolysis was slowly initiated under H_2 gas at a relatively high temperature. After the preheating step, the temperature was dramatically increased to approximately 950 °C. When the CVD furnace temperature reached 950 °C, the samples were placed on the heating zone for 1 h, and the heating zone with sulfur powder was turned on to initiate the sulfur sublimation. After 60 min of thermolysis, the furnace was cooled to room temperature at a rate of 10−15 °C/min under 40 and 200 sccm of H_2 and N_2 flow, respectively. The poly[methyl methacrylate] (PMMA) was then spin coated on the synthesized MoS_2 and WS_2 layers. For a fast separation between MeS_2 and the substrate, the edge of the substrate was scratched with a razor blade, and then immersed into a hydrogen fluoride and aluminum fluoride (1:1) bath at

room temperature for 1 h to etch away the SiO_2 layers. After that the remaining MoS_2 and WS_2 layers were carefully dipped into a DI water bath for 7−9 times to remove any residual etchant, the MoS_2 and WS_2 sheets were transferred to an arbitrary substrate. PMMA was removed by an acetone bath at 50 °C for 30 min after that the PMMA/MeS_2 layer had completely adhered to the target substrate.

Fabrication of the OLED. ITO glass was used as the starting substrate; its surface was cleaned in sequence with acetone, isopropyl alcohol, and DI water, and then dried with high purity nitrogen gas. After cleaning of substrate, the PEDOT:PSS or MeO_3 or MeS_2 layer were formed at the active area. The samples were treated with UV-O_3 for 3, 5, 7, and 9 min. Subsequently, they were loaded into the thermal evaporator where 40 nm of NPB was deposited. In a continuous process, Alq_3 (30 nm) doped with fluorescent dye 10-(2-benzothiazolyl)-2,3,6,7-tetrahydro-1,1,7,7-tetramethyl-1*H*,5*H*,11*H*-(1)-benzopyropyrano(6,7−8-i,j)quinolizin-11one (C545T) (1%), BCP (30 nm), LiF (1 nm), and Al (100 nm) layers were deposited in sequence. During the deposition, the base pressure of the chamber was maintained as low as 10^{-6} Torr. The active area of the device was 0.3 × 0.3 cm^2.

Fabrication of the OPV. The substrate preparation step was the same as that for the OLED fabrication procedure. After the HIL preparation step, the samples were treated with UV-O_3 and then loaded into a N_2-filled glovebox (<0.1 ppm of O_2 and H_2O). Regioregular P3HT (purchased from Rieke Metals and used as received) was first dissolved in 1,2-dichlorobenzene to make a 30 mg/mL solution, followed by blending with [6,6]-phenyl C_{61} butyric acid methyl ester ($PC_{61}BM$) (Nano-C, used as received) in a 3:2 weight ratio. The blend was stirred for approximately 12 h in a glovebox before being spin coated (700 rpm, 30 s) on top of the prepared substrate. The thickness of the active layer was approximately 160 nm, as measured by a surface profiler. The devices were annealed on a hot plate in a glovebox at 130 °C for 10 min. The cathode consisted of LiF (1 nm) and Al (100 nm) and was deposited at a base pressure of 1 × 10^{-6} Torr using a thermal evaporation method. The active device area was 0.3 × 0.3 cm^2.

Characterization. Raman spectra of synthesized MoS_2 and WS_2 were obtained with a Lab RAM HR (Horiba JobinYvon, Japan) at an excitation wavelength of 532 nm. SRPES experiments were performed in an ultrahigh vacuum chamber (base pressure of *ca.* 10^{-10} Torr) with a 4D beamline, equipped with an electron analyzer and heating element, at the Pohang Acceleration Laboratory. The onset of photoemission, corresponding to the vacuum level at the surface of the MoS_2 and WS_2 layers, was measured using the incident photon energy of 350 eV with a negative bias on the sample. The results were corrected for charging effects by using Au 4*f* as an internal reference. The current density−voltage and luminescence−voltage characteristics of the OLEDs and OPV cells were measured with a Keithley 2400 semiconductor parameter analyzer under ambient air conditions. The photocurrent of the OPV cells was measured under AM 1.5G 100 mW/cm^2 illumination with an Oriel 150 W solar simulator.

Conflict of Interest: The authors declare no competing financial interest.

Acknowledgment. This work was supported by Samsung Research Funding Center of Samsung Electronics under Project Number SRFC-MA1402-14.

Supporting Information Available: Figure S1 shows the surface treatment and solvent effect for the preparation of substrate. The photographic images of separated PMMA/MeS_2 layer on DI water and transferred MeS_2 on plastic films are shown in Figure S2. Figures S3−S5 show the SRPES survey scan, O 1*s* core level spectra, and the change of atomic concentration. The contact angle analysis is displayed in Figure S6. The AFM images are shown in Figure S7. Figure S8 shows the UPS data. The change of OLED device characteristics is summarized in Figures S9 and S10. The FE-SEM images are shown in Figure S11. The OPV device characteristics are shown in Figure S12. The total device data are summarized in Tabled S1−S4. This material is available free of charge *via* the Internet at http://pubs.acs.org.

REFERENCES AND NOTES

1. Wang, Q. H.; Kalantar-Zadeh, K.; Kis, A.; Coleman, J. N.; Strano, M. S. Electronics and Optoelectronics of Two-Dimensional Transition Metal Dichalcogenides. *Nat. Nanotechnol.* **2012**, *7*, 699–712.
2. Chhowalla, M.; Shin, H. S.; Eda, G.; Li, L.-J.; Loh, K. P.; Zhang, H. The Chemistry of Two-Dimensional Layered Transition Metal Dichalcogenide Nanosheets. *Nat. Chem.* **2013**, *5*, 263–275.
3. Chang, Y.-H.; Lin, C.-T.; Chen, T.-Y.; Hsu, C.-L.; Lee, Y.-H.; Zhang, W.; Wei, K.-H.; Li, L.-J. Highly Efficient Electrocatalytic Hydrogen Production by MoS_x Grown on Graphene-Protected 3D Ni Foams. *Adv. Mater.* **2013**, *25*, 756–760.
4. Bhandavt, R.; David, L.; Singh, G. Synthesis of Surface-Functionalized WS_2 Nanosheets and Performance as Li-Ion Battery Anodes. *J. Phys. Chem. Lett.* **2012**, *3*, 1523–1530.
5. Kim, S.; Konar, A.; Hwang, W.-S.; Lee, J. H.; Lee, J.; Yang, J.; Jung, C.; Kim, H.; Yoo, J.-B.; Choi, J.-Y.; *et al.* High-Mobility and Low-Power Thin-Film Transistors Based on Multilayer MoS_2 Crystal. *Nat. Commun.* **2012**, *3*, 1011.
6. Barga, D.; Lezama, I. G.; Berger, H.; Morpurgo, A. F. Quantitative Determination of the Band Gap of WS_2 with Ambipolar Ionic Liquid-Gated Transistors. *Nano Lett.* **2012**, *12*, 5218–5223.
7. Chang, J.; Register, L. F.; Banerjee, S. K. Atomistic Full-Band Simulations of Monolayer MoS_2 Transistors. *Appl. Phys. Lett.* **2013**, *103*, 223509.
8. Tongay, S.; Zhou, J.; Ataca, C.; Lo, K.; Mattews, T. S.; Li, J.; Grossman, J. C.; Wu, J. Thermally Driven Crossover from Indirect toward Direct Bandgap in 2D Semiconductors: $MoSe_2$ *versus* MoS_2. *Nano Lett.* **2012**, *12*, 5576–5580.
9. Zhao, W.; Ghorannevis, Z.; Chu, L.; Toh, M.; Kloc, C.; Tan, P.-H.; Eda, G. Evolution of Electronic Structure in Atomically Thin Sheets of WS_2 and WSe_2. *ACS Nano* **2013**, *7*, 791–797.
10. Xiao, D.; Liu, G.-B.; Feng, W.; Xu, X.; Yao, W. Coupled Spin and Valley Physics in Monolayers of MoS_2 and Other Group-VI Dichalcogenides. *Phys. Rev. Lett.* **2012**, *108*, 196802.
11. Zeng, Z.; Yin, Z.; Huang, X.; Li, H.; He, Q.; Lu, G.; Boey, F.; Zhang, H. Single-Layer Semiconducting Nanosheets: High-Yield Preparation and Device Fabrication. *Angew. Chem., Int. Ed.* **2011**, *50*, 11093–11097.
12. Coleman, J. N.; Lotya, M.; O'Neill, A.; Bergin, S. D.; King, P. J.; Khan, U.; Young, K.; Gaucher, A.; De, S.; Smith, R. J.; *et al.* Two-Dimensional Nanosheets Produced by Liquid Exfoliation of Layered Materials. *Science* **2011**, *331*, 568–571.
13. Seayad, A. M.; Antonelli, D. M. Recent Advances in Hydrogen Storage in Metal-Containing Inorganic Nanostructures and Related Materials. *Adv. Mater.* **2004**, *16*, 765–777.
14. Lee, Y.-H.; Zhang, X.-Q.; Zhang, W.; Chang, M.-T.; Lin, C.-T.; Chang, K.-D.; Yu, Y.-C.; Wang, J. T.-W.; Chang, C.-S.; Li, L.-J.; *et al.* Synthesis of Large-Area MoS_2 Atomic Layers with Chemical Vapor Deposition. *Adv. Mater.* **2012**, *24*, 2320–2325.
15. Zhang, Y.; Zhang, Y.; Ji, Q.; Ju, J.; Yuan, H.; Shi, J.; Gao, T.; Ma, D.; Liu, M.; Chen, Y.; *et al.* Controlled Growth of High-Quality Monolayer WS_2 Layer on Sapphire and Imaging Its Grain Boundary. *ACS Nano* **2013**, *7*, 8963–8971.
16. Najmaei, S.; Liu, Z.; Zhou, W.; Zou, X.; Shi, G.; Lei, S.; Yakobson, B. I.; Idrobo, J.-C.; Ajayan, P. M.; Lou, J. Vapour Phase Growth and Grain Boundary Structure of Molybdenum Disulphide Atomic Layers. *Nat. Mater.* **2013**, *12*, 754–759.
17. Liu, K.-K.; Zhang, W.; Lee, Y.-H.; Lin, Y.-C.; Chang, M.-T.; Su, C.-Y.; Chang, C.-S.; Li, H.; Shi, Y.; Zhang, H.; *et al.* Growth of Large-Area and Highly Crystalline MoS_2 Thin Layer on Insulating Substrates. *Nano Lett.* **2012**, *12*, 1538–1544.
18. Butler, S. Z.; Hollen, S. M.; Cao, L.; Cui, Y.; Gupta, J. A.; Gutiérrez, H. R.; Heinz, T. F.; Hong, S. S.; Huang, J.; Ismach, A. F.; *et al.* Progress, Challenges, and Opportunities in Two-Dimensional Materials beyond Graphene. *ACS Nano* **2013**, *7*, 2898–2926.
19. Jørgensen, M.; Norrman, K.; Krebs, F. C. Stability/Degradation of Polymer Solar Cells. *Sol. Energy Mater. Sol. Cells* **2008**, *92*, 686–714.

20. Tokarz-Sobieraj, R.; Hermann, K.; Witko, M.; Blume, A.; Mestl, G.; Scholögl, R. Properties of Oxygen Sites at the MoO_3 (010) Surface: Density Functional Theory Cluster Studies and Photoemission Experiments. *Surf. Sci.* **2001**, *489*, 107–125.
21. Anwar, M.; Hogarth, C. A.; Lott, K. A. K. Electron Spin Resonance Study of Thermally Evaporated Amorphous Thin Films of MoO_3/SiO. *Phys. Status Solidi A* **1989**, *114*, 225–231.
22. Elías, A. L.; Perea-López, N.; Castro-Beltrán, A.; Berkdemir, A.; Lv, R.; Feng, S.; Long, A. D.; Hyashi, T.; Kim, Y. A.; Endo, M.; *et al.* Controlled Synthesis and Transfer of Large-Area WS_2 Sheets: From Single Layer to Few Layers. *ACS Nano* **2013**, *7*, 5235–5242.
23. Brito, J. L.; Ilija, M.; Hernández, P. Thermal and Reductive Decomposition of Ammonium Thiomolybdates. *Thermochim. Acta* **1995**, *256*, 325–338.
24. van der Zande, A. M.; Huang, P. Y.; Chenet, D. A.; Berkelbach, T. C.; You, Y. M.; Lee, G.-H.; Heinz, T. F.; Reichman, D. R.; Muller, D. A.; Hone, J. C. Grains and Grain Boundaries in Highly Crystailline Monolayer Molybdenum Disulphide. *Nat. Mater.* **2013**, *12*, 554–561.
25. Yu, Y.; Li, C.; Liu, Y.; Su, L.; Zhang, Y.; Cao, L. Controlled Scalable Synthesis of Uniform, High-Quality Monolayer and Few-Layer MoS_2 Film. *Sci. Rep.* **2013**, *3*, 1866.
26. Mak, K. F.; Lee, C.; Hone, J.; Shan, J.; Heinz, T. F. Atomically Thin MoS_2: A New Direct-Gap Semiconductor. *Phys. Rev. Lett.* **2010**, *105*, 136805.
27. Yang, J.; Voriy, D.; Ahn, S. J.; Kang, D.; Kim, A. Y.; Chhowalla, M.; Shin, H. S. Two-Dimensional Hybrid Nanosheets of Tungsten Disulphide and Reduced Graphene Oxide as Catalysts for Enhanced Hydrogen Evolution. *Angew. Chem., Int. Ed.* **2013**, *52*, 13751–13754.
28. Lee, C.; Yan, H.; Brus, L. E.; Heinz, T. F.; Hone, J.; Ryu, S. Anomalous Lattice Vibrations of Single- and Few-Layer MoS_2. *ACS Nano* **2010**, *4*, 2695–2700.
29. Li, H.; Zhang, Q.; Yap, C. C. R.; Tay, B. K.; Edwin, T. H. T.; Oliver, A.; Baillargeat, D. From Bulk to Monolayer MoS_2: Evolution of Raman Scattering. *Adv. Funct. Mater.* **2012**, *22*, 1385–1390.
30. Berkdemir, A.; Gutiérrez, H. R.; Botello-Méndez, A. R.; Perea-López, N.; Elías, A. L.; Chia, C.-I.; Wang, B.; Crespi, V. H.; López-Urías, F.; Charlier, J.-C.; *et al.* Identification of Individual and Few Layers of WS_2 Using Raman Spectroscopy. *Sci. Rep.* **2013**, *3*, 1755.
31. Kwon, K. C.; Kim, S.; Kim, C.; Lee, J.-L.; Kim, S. Y. Fluropolymer-Assisted Graphene Electrode for Organic Light-Emitting Diodes. *Org. Electron.* **2014**, *15*, 3154–3161.
32. Le, Q. V.; Nguyen, T. P.; Jang, H. W.; Kim, S. Y. Use of UV/Ozone-Treated MoS_2 Nanosheets for Extended Air Stability in Organic Photovoltaic Cells. *Phys. Chem. Chem. Phys.* **2014**, *16*, 13123–13128.